Condensed Matter Physics, 2026, Vol. 29, No. 3, 33703: 1–14
DOI: 10.5488/CMP.29.33703
ISSN: 1607-324X https://cmpj2.icmp.lviv.ua

Computational investigation of a perovskite $LaBiO_3$ for photovoltaic, thermoelectric, and optoelectronic applications

M. M. Woldemariam, *N. G. Debelo, T. K. Tufa, E. M. Gurmesa, S. H. Didu, S. N. Asfaw, D. T. Keno

Department of Physics, Jimma University, P.O. Box 378, Jimma, Ethiopia

Received 06 February 2026; revised 04 June 2026; accepted 11 June 2026; published 28 September 2026

Using density functional theory (DFT) with the ONCVVPSP pseudopotential and PBE functional, this study investigates the structural, electronic, elastic, optical, and thermoelectric properties of the trigonal $LaBiO_3$ perovskite oxide (space group R3c). Ground-state parameters lattice constant, volume, bulk modulus, and its pressure derivative were determined using the equation of state. Applying the Hubbard correction (GGA+U) revealed an indirect, wide band gap of 3.51 eV. Mechanical properties, including the anisotropy factor, elastic modulus, and Poisson's ratio, were calculated via the Voigt–Reuss–Hill averaging scheme. The bulk-to-shear modulus ratio identifies the trigonal phase as ductile. Additionally, Debye temperatures and sound velocities were computed. Optical characteristics (absorption coefficient, refractive index, and electron energy loss function) were evaluated across a 0–35 eV spectral range. Finally, semi-classical transport coefficients, including electrical conductivity, Seebeck coefficient, and power factor, were calculated to assess the material's thermoelectric potential.

Key words: *DFT, $LaBiO_3$, electronic property, elastic property, optical property, transport property*

1. Introduction

Today, an increase in energy demand all over the world has prompted researchers to seek alternative materials that support clean and sustainable energy. Perovskite based materials have been established as a family of materials for light harvesting, energy conversion and storage [1–3]. In recent decades, inorganic-organic or organometal halide perovskites have gained prominence, although their origins trace back to the early 20th century. For the first time, the synthesis and physical properties of organometal lead halide perovskite was reported in 1970 [4]. Following this, the organometal lead halide perovskites have emerged as a candidate for solar cell absorbers with the first solar cell reported in 2009 [5]. Recently, the perovskite solar cells have attracted researchers due to a significant increase in power conversion efficiency from 3.8% to 25.5% [6].

Perovskite devices use light-absorbing materials with the perovskite crystal structure, generally expressed as ABX_3. In this structure, A and B are cations of different sizes, while X is typically an oxide or halide anion linking them [7, 8]. The A-site cations, usually larger and lower in valence such as Ca or La occupy 12-fold oxygen-coordinated positions. Smaller B-site cations, including Co or Cr, sit in six-fold octahedral coordination. Both sites can be modified by substituting metals or semi-metals. When lower-valence cations replace A or B, the charge imbalance creates oxygen vacancies. These vacancies enable mixed ionic-electronic conductivity, mainly governed by transition-metal centers, and help maintain the charge neutrality within the lattice [9, 10].

Despite the growing interest in organic halide perovskite materials, significant challenges remain before they can be broadly adopted for large-scale commercial applications. One major concern is the presence of toxic lead (Pb), which poses environmental and health risks. Additionally, these materials

*Corresponding author: menberu.mengesha@ju.edu.et

are highly sensitive to moisture, leading to rapid degradation [11], and they suffer from ion migration, which raises concerns about long-term stability [12]. Their ultralow thermal conductivity also contributes to potential heating and mechanical stress during operation [13]. Whereas ongoing research is making progress in addressing some of these issues, others may be inherent to the nature of organic lead halide perovskites and therefore difficult to overcome.

Perovskite oxides have garnered a considerable scientific attention because of their diverse and flexible potential applications. These materials are being explored across various applications, including fuel cells, power generation, magnetic sensors, spintronics, actuators, high-pressure magnetic and optical sensors, supercapacitors, high-strength composites, radiation tracers, piezoelectric and thermoelectric material. This broad applicability has driven extensive research efforts aimed at unlocking their full potential [14, 15].

To our understanding, the structural, electronic, elastic, optical, and thermoelectric properties of $LaBiO_3$ have not been thoroughly investigated using first-principles methods. We assessed their structural stability using the commonly employed octahedral and Goldschmidt tolerance factors. The electronic properties are calculated by considering GGA-PBE [17] as well as density functional theory (DFT) with the Hubbard functional (GGA+U) [18] for exchange correlation potential using Quantum Espresso Package (QE). The thermodynamic properties are calculated using the thermo-pw software interfaced with Quantum Espresso [22]. Moreover, the optical properties were evaluated using time-dependent density functional perturbation theory (TD-DFPT) within the independent-particle formalism and the random phase approximation. In addition, the semi-classical transport coefficients are determined within the Boltzmann transport theory using BoltzTrap code [23]. Overall, with such predictable properties, these materials hold a considerable potential for thermoelectric and optoelectronic applications, albeit requiring experimental confirmation.

2. Computational details

In this work, the first principle computations were performed within Quantum Espresso software Package (QE) [16] based on the density functional theory (DFT) as implemented within the generalized gradient approximation (GGA) with the Hubbard correction (GGA+U) [18]. The effective Hubbard parameter (U_{eff}) was calculated iteratively for La-5d orbital using a linear response formalism utilizing DFPT with ortho-atomic projection method [19] and found $U_{\text{eff}} = 1.65$ for La (d). The optimized norm-conserving Vanderbilt pseudopotential (ONCVPSP) with Perdew-Burke-Ernzerhof (PBE) exchange-correlation functional were used to treat the interaction of the electrons with the ion cores as in [19]. For the calculations, the relevant valence electrons are La-[Xe]$5d^1 6s^1$, Bi-[Xe]$4f^{14} 5d^{10} 6s^2 6p^2$, O-[He]$2s^2 2p^4$. Careful tests were performed to ensure the convergence of calculations concerning the plane-wave cut-off and k-point mesh. Crystal structure optimization is done using a plane wave cutoff energy of 60 Ry and the Brillouin zone with an $8 \times 8 \times 8$ Monkhorst-Pack k-point grid [20] based on the convergence criteria — energy 10^{-5} Ry, force 10^{-3} Ry/Bohr, and cell pressure 0.5 kbar — with the help of Brodyden–Fletcher–Goldfarb–Shanno (BFGS) method [21]. Thermodynamic properties were calculated using Thermo-pw code [22]. The semi-classical transport coefficients were obtained by converting the Quantum Espresso output generated with a dense k-point mesh into a format compatible with the BoltzTraP code [23].

3. Result and discussions

3.1. Structure properties

In this study, the trigonal structure of $LaBiO_3$ [with space group R3c (161)], was considered as shown in figure 1. In the trigonal structure of $LaBiO_3$, both La^{3+} and Bi^{3+} cations are coordinated to six oxygen atoms forming distorted octahedra. Unlike the corner sharing network found in cubic perovskites, these LaO_6 and BiO_6 units are aranged in a more densely packed framework characterized by edge sharing and face sharing connectivity. Especially, the Bi^{3+} ion is coordinated to six equivalent O^{2-} atoms, resulting in

a distorted BiO_6 octahedron where the distortion is derived by the streochemical activity of the bismuth $6s^2$ lone pair. The La^{3+} ion is surrounded by six equivalent O^{2-} atoms, where the La–O bonds measure 2.43 Å, the Bi–O bond length is 2.11 Å and the La–Bi measure 3.2 Å.

The Goldschmidt factor is a crucial parameter for providing structural information on perovskites. The modified form of Goldschmidt tolerance factor (τ) is given by [24]:

$$\tau = \frac{1}{\sqrt{2}} \frac{(r_{La} + r_O)}{(r_{Bi} + r_O)}, \tag{3.1}$$

where r_{La}, r_{Bi} and r_O are ionic radii, respectively.

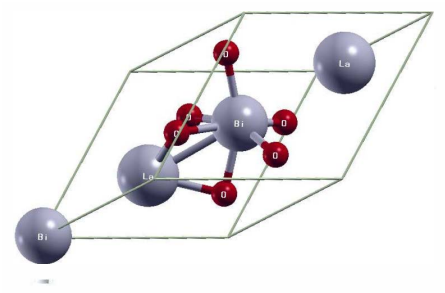

Figure 1. (Colour online) Crystallographic structures of R3c $LaBiO_3$.

Typically, a tolerance factor of 0.9–1.0 produces an ideal cubic arrangement, while a factor between 0.71 and 0.9 induces a distorted perovskite structure featuring tilted octahedra. Non-perovskite structures are formed when the tolerance factor is higher (> 1) or lower (< 0.71) [24]. La^{3+} exhibits a calculated tolerance factor of 0.81, which verifies the stability of a cubic perovskite structure, as displayed in table 1.

Table 1. The ionic radii and calculated tolerance factor of $LaBiO_3$.

Ions	Ionic radius (Å)	Tolerance factor
La^{+3}	1.36	
Bi^{+3}	1.02	0.81
O^{-2}	1.4	

In this study, the structural stability and total energy as a function of atomic volume for La^{3+} were investigated through total energy minimization using PBE-GGA and GGA+U exchange-correlation functionals. From the optimized geometry, the lattice constant is calculated as 11.3 a.u. using GGA-PBE and 11.6 a.u. using GGA+U. The equilibrium lattice potential, related to the total energy, was evaluated via a set of strained lattice configurations. These findings enable the calculation of the equilibrium unit cell volume (V_0), bulk modulus (B_0), and its pressure derivatives (B_0'). A series of volume-dependent total energy calculations can be fitted to an equation of state consistent with Murnaghan equation of state (energy versus volume) [25] as

$$E(V) = E_0 + \frac{B_0 V}{B_0'} \left[\frac{(V_0/V)^{B_0'}}{B_0' - 1} + 1 \right] - \frac{B_0 V_0}{B_0' - 1}, \tag{3.2}$$

where B_0 is an equilibrium bulk modulus that effectively measures the curvature of the energy versus the volume curve about the relaxed volume V_0, and B_0' is the derivative of the bulk modulus. The calculated total energy is fitted into the Murnaghan equation [25] for a number lattice constant demonstrated as shown in figure 2. The computed values of the unit cell volume (V_0), bulk modulus (B_0), and its pressure derivative (B_0') are presented in table 2. Furthermore, the results indicate that the GGA+U approximation

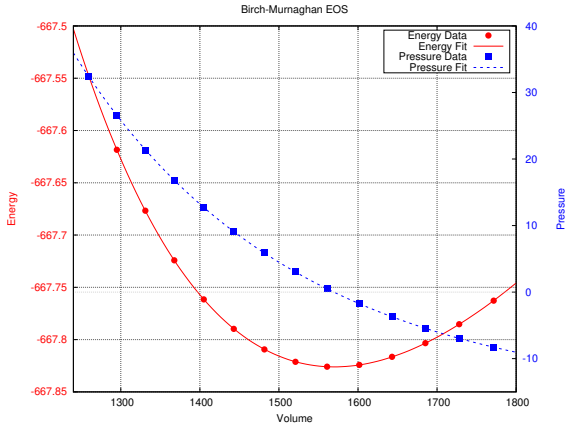

Figure 2. (Colour online) Volume versus energy and pressure.

yields a lower bulk modulus and its derivative, along with an increase in the lattice constants and volume, compared to those obtained using GGA-PBE.

The formation energy of compound is among the most crucial parameters determining its stability. The higher are the negative values of the formation energy, the more stable the compound is predicted to be [26]. The formation energy, ΔH, for this system as in [27] can be calculated as:

$$\Delta H(\mathrm{LaBiO_3}) = \{E_{\mathrm{tot}}(\mathrm{LaBiO_3}) - [N_{\mathrm{La}}E_{\mathrm{tot}}(\mathrm{La}) + N_{\mathrm{Bi}}E_{\mathrm{tot}}(\mathrm{Bi}) + N_{\mathrm{O}}E_{\mathrm{tot}}(\mathrm{O})]\}\frac{1}{N_{\mathrm{tot}}}, \tag{3.3}$$

where N_{La}, N_{Bi}, and N_{O} are total numbers of La (= 1), Bi (= 1), and O (= 3) atoms respectively, and N_{tot} is total number of atoms in $\mathrm{LaBiO_3}$ (= 5). The formation energy is determined and given in table 2. The negative values indicate that the energy gained during the formation confirms that the compounds are stable.

Table 2. Calculated values of equilibrium lattice constant, unit cell volume, bulk modulus and its derivative of $\mathrm{LaBiO_3}$ in comparison with existing works.

Source	Phase	a (a.u.)	Vol (a.u.^{3})	B (GPa)	B'	ΔH (eV/atom)
GGA-PBE	Fm-3m	11.3	1442.89	91	4.31	–2.6343
GGA+U		11.6	1560.89	89	4.24	–

3.2. Elastic properties

Mechanical properties

The elastic constants of a material define its mechanical behavior. They offer crucial insights into the properties such as mechanical stability, brittleness, ductility, rigidity, elastic moduli, Poisson's ratio, and the elastic anisotropy of materials. The complete elastic constant tensor was determined from calculations of the stresses induced by slight deformations of the equilibrium primitive cell and thus, the elastic constants C_{ijk} are determined as [28, 29].

$$C_{ijkl} = \left.\frac{\partial \sigma_{ij}}{\partial \varepsilon_{kl}}\right|_{\chi} = \frac{1}{V}\left.\frac{\partial^2 E}{\partial \varepsilon_{ij}\partial \epsilon_{kl}}\right|_{\chi}, \tag{3.4}$$

where E denotes the Helmholtz free energy, ε_{ij} and ε_{kl} represent the imposed stress and Eulerian strain tensors, respectively, and χ refers to the coordinate variables.

For the case of trigonal crystal, there are six independent elastic constants ($C_{11}, C_{12}, C_{13}, C_{14}, C_{33}$, and C_{44}) that should satisfy the six well-known mechanical stability criteria [30]

$$C_{11} - C_{12} > 0, \quad (C_{11} + C_{12})C_{33} - 2C_{13}^2 > 0, \quad (C_{11} - C_{12})C_{44} - 2C_{14}^2 > 0. \tag{3.5}$$

These criteria ensure that the crystal will not undergo any spontaneous deformation under small perturbations, indicating a mechanical stability. If any of these conditions are violated, the crystal is likely to be unstable under elastic deformations.

The elastic constants calculated for a trigonal structure R3c (161) $LaBiO_3$ were found to be C_{11} = 216.15 GPa, C_{12} = 127.8 GPa, C_{13} = 73.05 GPa, C_{14} = 5.10 GPa, C_{33} = 96.99 GPa, C_{44} = 39.67 GPa, and C_{66} = 44.17 GPa with GGA+U approximation that satisfy the above mechanical stability conditions. From the calculated elastic constants, the mechanical parameters such as the Young modulus (E), shear modulus (G), Poisson's ratio (η), and Pugh ratio (r) are determined by using the Voigt–Reuss–Hill (VRH) average approximation [31].

The upper limit and lower limit of the actual effective modulus correspond to the Voigt bound based on uniform strain throughout a polycrystalline assumption and the Reuss bound based on the uniform stress throughout a polycrystalline assumption obtained by the average polycrystalline modulus [32]. For trigonal lattices, Voigt bulk modulus (B_V) and shear modulus (G_V) are

$$B_V = \frac{1}{9}[2(C_{11}+C_{12})+4C_{13}+C_{33}], \quad G_V = \frac{1}{15}[2C11-C_{12}+C_{33}-2C_{13}+6C_{44}+3(C_{11}-C_{12})/2], \tag{3.6}$$

and the Reuss bulk modulus (B_R) and the Reuss shear modulus (G_R) are described as:

$$B_R = \frac{(C_{11} + C_{12})C_{33} - 2C_{13}^2}{C_{11} + C_{12} + 2C_{33} - 4C_{13}}, \quad G_R = \frac{15}{4(2S_{11} + S_{33}) - 4(S_{12} + 2S_{13}) + 3(2S_{44} + S)}, \tag{3.7}$$

where S_{ij} are the compliance constants. The Voigt and Reuss schemes establish the theoretical maximum and minimum limits of the real polycrystalline elastic parameters. Therefore, the practical approximation of the bulk and shear moduli can be considered as the arithmetic mean of the two extremes [33]. The Hill's average for the shear modulus (G) and bulk modulus (B) is described by

$$G = \frac{1}{2}(G_V + G_R), \quad B = \frac{1}{2}(B_V + B_R), \tag{3.8}$$

where B_R and G_R are the Reuss bulk and shear moduli, and B_V and G_V correspond to the Voigt bulk and shear moduli. Moreover, the Young modulus (E), Poisson's ratio (η), anisotropic index (A^I) are given by [29, 32, 33]

$$E = \frac{9BG}{3B + G}, \quad \eta = \frac{3B - 2G}{2(3B + G)}, \quad A^I = 5\frac{G_V}{G_R} + \frac{B_V}{B_R} - 6. \tag{3.9}$$

Table 3. Mechanical properties calculated from the elastic constants of $LaBiO_3$.

Source	B_V	G_V	B_R	G_R	B	E	G	η	r	A^I
GGA+U	119.76	41.81	92.33	38.12	106.045	106.52	39.98	0.33	0.38	0.78

The calculated Bulk modulus is 109.16 GPa using the GGA+U exchange correlation functional. The bulk modulus values derived from elastic constants (table 3) and from the equation of state (table 2), obtained with GGA+U (91 GPa), show a close agreement with only minor variation. The ductile or brittle nature of a metallic material directly governs its mechanical behavior and likewise dictates its mode of failure. Pugh et al. [34] introduced the ratio of bulk modulus to shear modulus B/G (2.64) as a reference for the judgment of the ductility of a material. For a normal material, if its B/G value exceeds 1.75, the material is ductile, otherwise it is brittle [35]. From table 3, the calculated B/G ratio (GGA+U) for the trigonal R3c (161) $LaBiO_3$ structure indicates that the material posesses good ductile behavior.

Furthermore, Poisson's ratio (η) serves as a mechanical indicator that provides a valuable insight into the nature of the bonding forces. In the evaluation of Poisson's ratio, 0.25 and 0.5 are the lower and upper limits of the central force, respectively [35]. From table 3, the Poisson's ratio (η) obtained using the GGA+U approach is 0.33, which falls within the expected bounds and signifies that the interatomic bonding forces are predominantly central in nature. The universal anisotropic index (A^I) is a measure to quantify the elastic anisotropic characteristics based on the contributions of both bulk and sheared moduli [34]. Its value equals zero for a perfectly isotropic material. When ($A^I \neq 0$), the magnitude of its value reflects the degree of elastic anisotropy, with any positive or negative deviation from zero indicating an increased level of anisotropy. The computed universal anisotropic index (A^u) for trigonal structure $LaBiO_3$ is 0.78 with GGA+U, indicating the anisotropic property.

Thermodynamic properties

One of the fundamental properties of materials, the Debye temperature (θ_D), correlates with many physical properties of solids such as specific heat, elastic constant and melting temperature [33]. One of the known approaches to calculate the Debye temperature (θ_D) can be estimated from the averaged sound velocity (C_m) and is given by [35]

$$\theta_D = \frac{h}{k_\mathrm{B}}\left[\frac{3n}{4\pi}\left(\frac{N_\mathrm{A}\rho}{M}\right)\right]^{\frac{1}{3}} C_m, \tag{3.10}$$

where h is Plank's constant, k_B is Boltzmann's constant, N_A is Avogadro's number, ρ is density, M is molecular weight and n is the number of atoms in a formula unit. Then, C_m is

$$C_m = \left[\frac{1}{3}\left(\frac{2}{c_t^3} + \frac{1}{c_l^3}\right)\right]^{-\frac{1}{3}}, \tag{3.11}$$

where c_l and c_t are the longitudinal and transverse sound velocity. These velocities can be obtained from density, shear and bulk modulus of the material as:

$$c_l = \left(\frac{B + \frac{4}{3}G}{\rho}\right)^{\frac{1}{2}}, \tag{3.12}$$

$$c_t = \left(\frac{G}{\rho}\right)^{\frac{1}{2}}. \tag{3.13}$$

Using a relaxed unit cell volume of 1042.064 a.u.^{3} (1.544×10^{-22} cm^3) from the Quantum ESPRESSO output, the calculated mass density of $BaTiO_3$ is 8.54 g·cm^{-3} (8.54×10^3 kg·m^{-3}). This value was derived using the standard relation between unit-cell mass and volume, which incorporates the atomic masses of Ba, Ti, and O.

Based on the determined elastic constants and density, the derived longitudinal c_l and transverse c_t sound velocities, the average sound velocity C_m, and the Debye temperature θ_D for $LaBiO_3$ are presented in table 4.

Table 4. Computed parameters of sound velocities, and Debye temperature of $LaBiO_3$.

Sourse	c_l (m/s)	c_t (m/s)	C_m (m/s)	θ_D (K)
Calculated value (GGA+U)	4322.63	2171.10	2405.32	288.82

The thermodynamic properties of the perovskite structure were further examined using the quasi-harmonic Debye model [38]. In this framework, the nonequilibrium Gibbs free energy $G(V,P,T)$ is described by:

$$G(V;P,T) = E(V) + PV + F_{vib}[\theta_D(V);T]. \tag{3.14}$$

Here, $E(V)$ represents the total energy per unit cell, PV stands for the applied hydrostatic pressure, $\theta(V)$ denotes the Debye temperature as a function of volume, and F_{vib} corresponds to the vibrational Helmholtz free energy. Within the quasi-harmonic Debye model, which incorporates the phonon density of states, the vibrational Helmholtz free energy F_{vib} is expressed as [38, 39]:

$$F_{vib}(\theta_D;T) = nk_{\mathrm{B}}T\left[\frac{9\theta}{8T} + 3\ln\left(1-\mathrm{e}^{-\theta/T}\right) - D\left(\frac{\theta_D}{T}\right)\right], \tag{3.15}$$

where n is the number of atoms per formula unit, $D(\theta_D/T)$ denotes the Debye integral. For an isotropic solid, θ_D can be expressed as [30, 32]

$$\theta_D = \frac{\hbar}{k_{\mathrm{B}}}(6\pi^2V^{1/2}n)^{1/3}f(\sigma)\sqrt{B_s/M}. \tag{3.16}$$

Here, M is the molecular mass per unit cell and B_s is the adiabatic bulk modulus, which characterizes the compressibility of the crystal and is approximated by the static compressibility as [30]:

$$B_s \cong B(V) = V\frac{\mathrm{d}^2E(V)}{\mathrm{d}V^2}. \tag{3.17}$$

Heat capacity at constant volume C_v, and the entropy are expressed by

$$C_v = 3nk_{\mathrm{B}}\left[4D\left(\frac{\theta_D}{T}\right) - \frac{3\theta_D/T}{\mathrm{e}^{\theta_D}-1}\right], \tag{3.18}$$

$$S = nk_{\mathrm{B}}\left[4D\left(\frac{\theta}{T}\right) - 3\ln\left(1-\mathrm{e}^{-\frac{\theta}{T}}\right)\right]. \tag{3.19}$$

We evaluated the thermodynamic properties of $LaBiO_3$ including enthalpy, Gibbs free energy, entropy, and heat capacity over the temperature range of 0–800 K, as presented in figure 3. For the analysis, both volume and temperature were considered as independent variables. As demonstrated in figure 3, the entropy and heat capacity approach zero at 0 K, which is consistent with the third law of thermodynamics. As temperature rises, the Gibbs free energy decreases gradually, whereas the entropy increases sharply. These trends are consistent with previously reported results in [32, 33]. Consequently, the enthalpy rises nearly linearly with temperature. At higher temperatures, this increment in enthalpy contributes to a reduction in the defect-related free energy. The heat capacity increases sharply below 200 K and then approaches the classical Dulong–Petit limit 500 $\mathrm{K^{-1}mol^{-1}}$ above 200 K. This trend is consistent with anharmonic corrections within the Debye model, as reported in [35, 36]. Moreover, the smooth and continuous variation in heat capacity indicates the absence of any phase transitions up to 800 K, in agreement with reference [30]. Overall, these results provide useful insights for future studies.

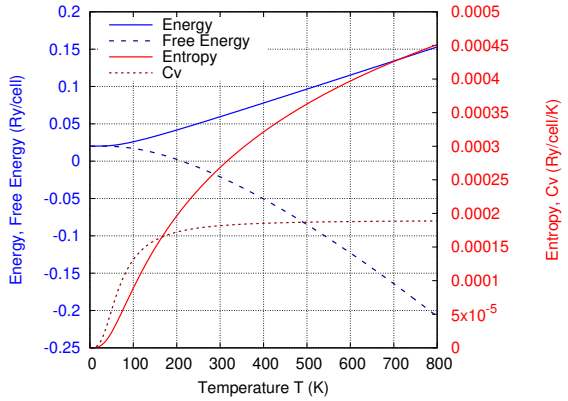

Figure 3. (Colour online) Debye vibrational energy, free energy, heat capacity, and entropy.

3.3. Electronic parameters: band structure and density of states

The density of states and electronic band structure typically offer an appropriate information for a comprehensive characterization of electronic properties of a material. In this work, the electronic band structure and density states of $LaBiO_3$ along the high-symmetry directions of the Brillouin zone are calculated using the GGA and GGA+U approach for the exchange-correlation potential, as illustrated in figure 4. The calculated band structure shows that the trigonal phase of $LaBiO_3$ is an indirect large band gap material. Using the GGA and GGA+U exchange-correlation potential, the computed energy gap values for trigonal $LaBiO_3$ are 3.48 eV and 3.54 eV, respectively. The band gap value obtained by GGA+U for exchange correlation potential is somewhat larger than the value calculated using GGA approximation.

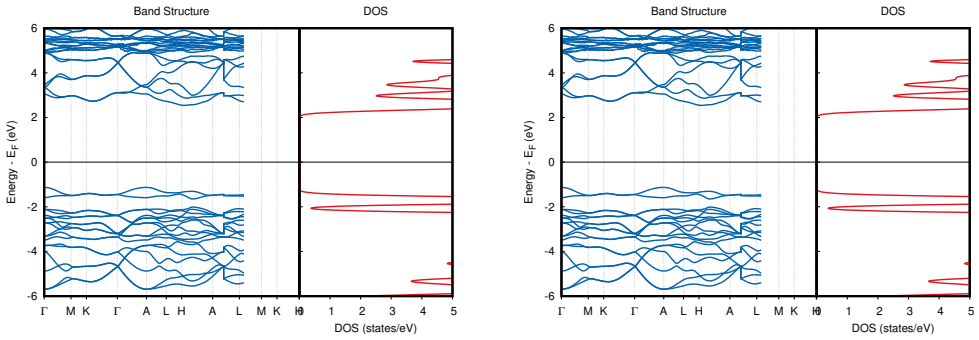

Figure 4. (Colour online) Band structure and density state of $LaBiO_3$ with respect to GGA-PBE (left-hand) and GGA+U (right-hand).

3.4. Optical properties

To compute the optical properties, the complex dielectric function $\varepsilon(\omega)$ is employed within an adiabatic exchange correlation functionals (AXCA) [40]. The imaginary component, $\varepsilon_2(\omega)$, is determined from the dipole transition matrix elements between valence and conduction band states, employing the long-wavelength approximation. The dispersion of the real part of the dielectric function $\varepsilon_1(\omega)$ was determined from the imaginary part using the Kramers-Kronig relations. Furthermore, the experimentally accessible optical parameters such as the refractive index $\mathrm{Re}[\varepsilon_M(\omega)]_{q\to 0}$, the absorption coefficient $\mathrm{Im}[\varepsilon_M(\omega)]_{q\to 0}$, and the energy loss function $-\mathrm{Im}\,[1/\varepsilon_M(\omega)]_{q\to 0}$, are explored in trigonal structure of $LaBiO_3$. The calculated optical properties are demonstrated in figure 5.

In figure 5, the absorption coefficient for $LaBiO_3$ shows a maximum peak at 10 eV, attributed to single excitation. By contrast, the peak in the electron energy loss function (EELF), associated with collective plasmon excitation, occurs at a higher energy of 30 eV. The maximum of the electron energy loss function is observed when $\mathrm{Re}\,\varepsilon_M(\omega) = 0$ and $\mathrm{Im}\,\varepsilon_M(\omega)$ is small. The imaginary component $\varepsilon_2(\omega)$ of the dielectric function governs the optical transition processes, with each peak representing a specific electronic transition.

At low energy range (0–10 eV), the optical properties clearly describe the system as shown in figure 6. The real part $\mathrm{Re}\,\varepsilon_M(\omega)$ describes the refractive index of the material and how much it slows down the light. The anomalous dispersion is observed around 6 eV and 9 eV. At the far right (10 eV), the value drops below zero which usually indicates the onset of plasma-like behavior. The imaginary part $\mathrm{Im}\,\varepsilon_M(\omega)$ represents the energy absorption and $LaBiO_3$ is transparent until about 3.6 eV due to its wide band gap. The peaks at 6.2 eV and 9.5 eV correspond to specific electronic transitions from valence band to conduction band.

The electron energy loss function $-\mathrm{Im}\,[1/\varepsilon_M(\omega)]$ describes how much energy an electron loses as it passes through the bulk of the material. Peaks in this line (10 eV) typically identify plasmone. How the absorption constant and a refractive index changes with respect to photon enegy is described in table 5.

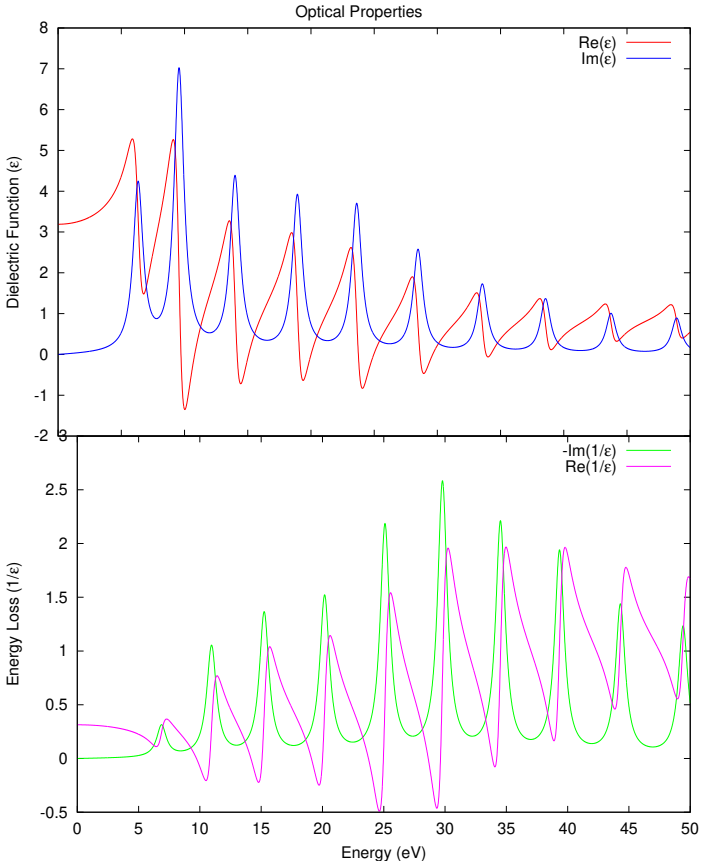

Figure 5. (Colour online) The real and imaginary part of macroscopic dielectric function, and the electron energy loss function as function of energy.

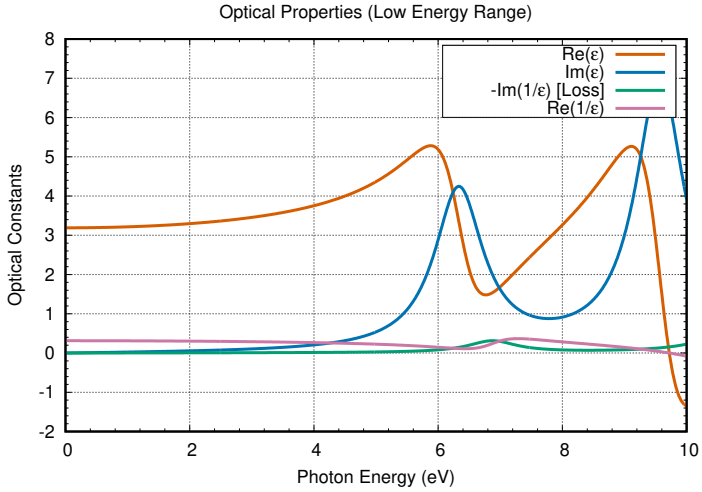

Figure 6. (Colour online) Absorption coefficient of $LaBiO_3$ at low energy regime

Moreover, the absorption coefficient of trigonal $LaBiO_3$ is determined using independent particle approximation (without considering electron interaction) and including electron interactions (Hartree and exchange correlation effects) as shown in figure 7. The red shift of the peak is observed in the

Table 5. Calculated values for the real and imaginary parts of the dielectric function and the refractive index at selected photon energies $LaBiO_3$.

Photon energy (E)	Re $\varepsilon_M(\omega)$	Im $\varepsilon_M(\omega)$	Calculated refractive index $n(\omega)$
2.0 eV (visible range)	3.3	0.0	1.82
4.0 eV (near UV)	3.8	0.3	1.95
6.0 eV (resonance peak)	5.3	3.5	2.8
10.0 eV (high energy)	−1.4	3.8	1.15

absorption coefficient when electron-electron interaction is considered. Moreover, the absorption spectra are quenched due to the local field effects.

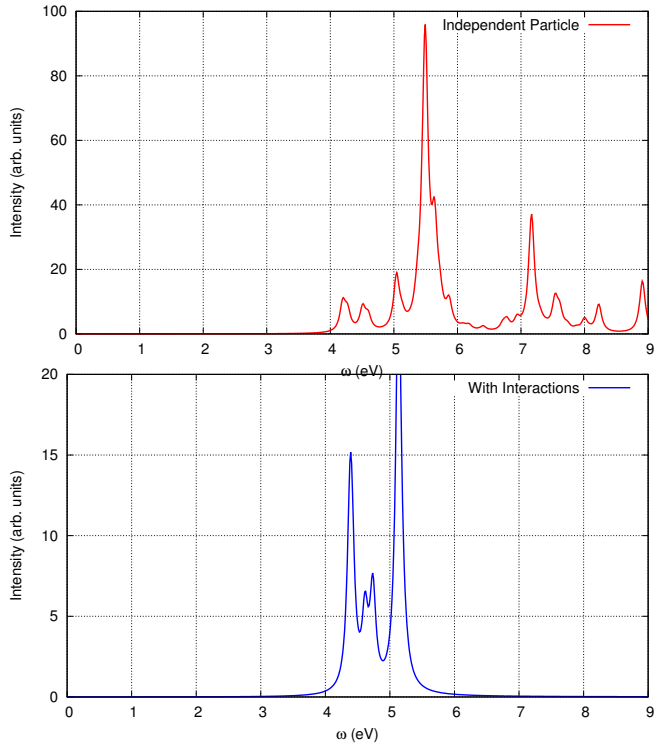

Figure 7. (Colour online) Absorption coefficient of $LaBiO_3$ with no interaction and including electron interactions.

3.5. Transport properties

Boltzmann transport theory based on the first-principles electronic structure calculations was employed to determine the semi-classical transport coefficients. In this transport property investigation, only the electronic contribution is considered. This approach helps to evaluate the temperature dependence of the power factor (PF), electrical conductivity per relaxation time (σ/τ), and Seebeck coefficient (S). The resulting transport coefficients for $LaBiO_3$ are presented in figure 8 .

In figure 8 (top) the Seebeck coefficient increases considerably as Fermi energy is shifted towards the p-type region. Moreover, its magnitude increases with an increment of temperature. Particularly, strong thermopower especially in the p-type side indicates that $LaBiO_3$ has favorable thermoelectric behavior.

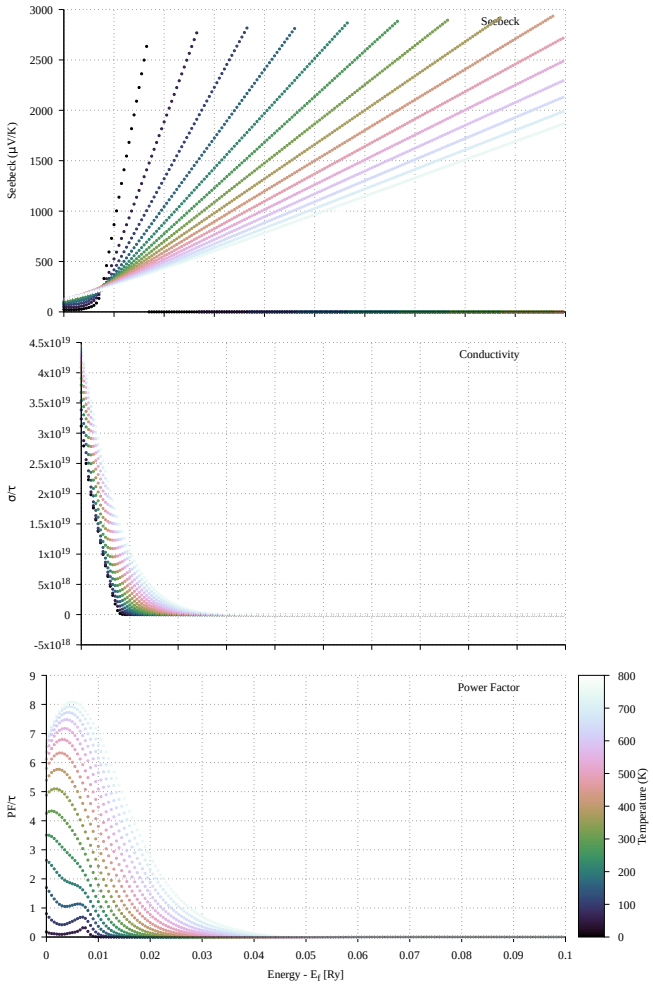

Figure 8. (Colour online) [Top] Power factor per relaxation time (10^{11} W/m·K^2·s), [middle] conductivity per relaxation time ($10^{19}/\Omega$·cm·s), and [bottom] Seebeck (μV/K) as a function of energy $[E - E_F]$ (Ry) for different temperatures 50–800 K with step of 50 K.

Figure 8 (middle) describes a strong peak of electrical conductivity per relaxation time near the Fermi level ($E - E_F = 0$), and then rapidly drops. This is attributed to the high density of states near the Fermi level, which enhances the carrier concentration and, consequently, the conductivity. As the carrier density decreases further from the Fermi energy, the conductivity per relaxation time (σ/τ) drops accordingly. The result indicates that $LaBiO_3$ becomes more conducting near the intrinsic Fermi level. Figure 8 (bottom) reveals that the PF initially rises as the Fermi level moves away from the reference point (towards p-type region). It reaches a maximum for each temperature and then sharply decreases. Higher temperatures ($\geqslant$ 600 K) show a larger peak of PF, which indicates a better thermoelectric performance at higher temperature. Moreover, at a specific temperature of 600 K, the estimated relaxation time τ is 10^{-14} s, while the computed maximum conductivity per relaxation time σ/τ is 4.3×10^{19} $(\Omega\cdot\text{cm}\cdot\text{s})^{-1}$. By combining these parameters, the resulting electrical conductivity σ is determined to be 4.3×10^5 $(\Omega\cdot\text{cm})^{-1}$, a value that indicates high conductivity for the material under these specific thermal conditions. Thus, $LaBiO_3$ shows promise for thermoelectric applications especially in p-type regime at elevated temperatures. The transport coefficients as a function of temperature are described in figure 9.

The transport properties indicate that the material is a p-type semiconductor, as evidenced by the positive Seebeck coefficient which rises from 20 μV/K and plateaus near 125 μV/K at higher temperatures.

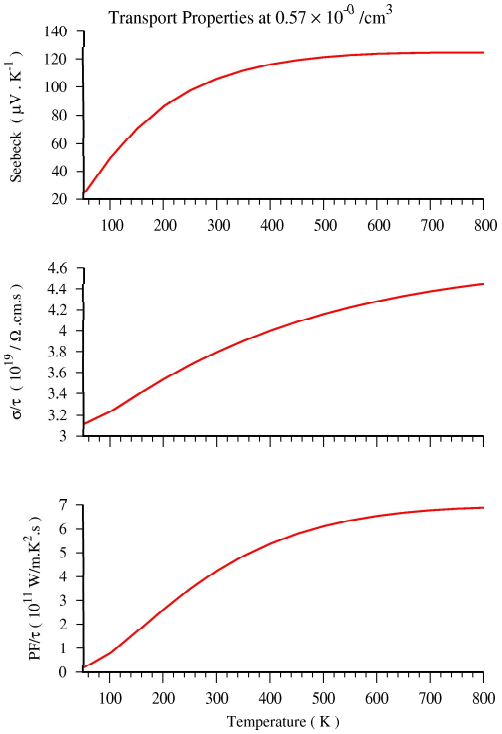

Figure 9. (Colour online) [Top] Seebeck (μV/K), [middle] conductivity per relaxation time ($10^{19}/\Omega{\cdot}\text{cm}{\cdot}\text{s}$), and [bottom] power factor per relaxation time (10^{11} W/m·K^2·s) as a function of temperature.

Both the scaled electrical conductivity (σ/τ) and the scaled power factor (PF/τ) exhibit a steady monotonous increase across the temperature range from 50 K to 800 K, suggesting that the electronic performance of the material is optimized for high-temperature applications. Specifically, the sharp upward trajectory of the power factor, driven by the squared relationship with the Seebeck coefficient (S^2), indicates that the material reaches its maximum thermoelectric efficiency at approximately 800 K, where it reaches its peak value of 7×10^{11} W/(m·K^2·s).

In conclusion, $LaBiO_3$ demonstrates a promising thermoelectric performance, particularly under p-type doping and high temperatures ($\geqslant$ 500 K). Enhanced power factor and Seebeck coefficient at elevated temperatures indicate suitability for waste heat energy conversion and thermoelectric devices.

4. Conclusion

The structural, electronic, elastic, thermodynamic, optical and thermoelectric parameters of trigonal $LaBiO_3$ perovskite were investigated via first-principles calculations employing the Quantum Espresso package. Using the GGA-PBE functional, the lattice parameter was computed as 11.3 Bohr, while the GGA+U method yielded 11.6 Bohr. The formation energy is determined and its value is −2.6343 eV/atom (negative values) indicating that the energy gained during the formation confirms that the compounds are stable. The elastic constants of $LaBiO_3$ were determined and employed to evaluate the mechanical properties, including the bulk modulus, shear modulus, Young's modulus, and elastic anisotropy. Using GGA+U, the Poisson's ratio is found to be 0.33, suggesting that the interatomic forces are predominantly central. The computed B/G ratio of 2.7 using GGA+U confirms that $LaBiO_3$ exhibits a ductile behavior. The band gap value was calculated using GGA+U approximation for the exchange correlation potential. The band gap obtained using the Hubbard-corrected GGA+U method for on-site interactions is 3.51 eV. Optical properties, including the absorption coefficient, refractive index, and electron energy loss function,

were calculated and analyzed in detail. The Hartree and exchange correlation effect in absorption spectra results in blue shift of the peak. Moreover, the absorption spectra are quenched due to the local field effect when the electron-electron interaction is considered. Finally, the semi-classical transport coefficients were calculated, and they demonstrate that $LaBiO_3$ may be suitable for waste heat energy conversion and thermoelectric devices. It can also be used for photocatalysis, for energy conversion and storage.

Acknowledgements

This study was supported by a staff research grant from the College of Natural Sciences, Jimma University. The authors would like to acknowledge CHPC LENGAU South Africa for High Performance Cluster Machine (HPC) support during the computation.

References

1. Kumar S., Sharma V., Kumari N., Kaur G. A., Saha A., Thakur S., Shandilya M., Ionics, 2024, **30**, 5159, doi:10.1007/s11581-024-05658-3.
2. Jamesh M. I., Tong H., Du M., Niu W., Jia G., Cheng K.-C., Hsieh C.-W., Shen H.-H., Xu B., Tian Y., Xu X., Hsu H.-Y., npj Mater. Sustainability, 2025, **3**, 29, doi:10.1038/s44296-025-00073-9.
3. Kumar V., Singh S., Appl. Surf. Sci., 2016, **386**, 78, doi:10.1016/j.apsusc.2016.05.163
4. Dieter W., Z. Naturforsch. B, 1978, **33**, 862, doi:10.1515/znb-1978-0809.
5. Kojima A., Teshima K., Shirai Y., Miyasaka T., J. Am. Chem. Soc., 2009, **131**, 6050, doi:10.1021/ja809598r.
6. Ivanova A. S., Khanina A. S., Gostishchev P. A., Saranin D. S., Nanobiotechnol. Rep., 2024, **19**, S1, doi:10.1134/S2635167624602754.
7. Akkerman Q. A., Manna L., ACS Energy Lett., 2020, **5**, 2, doi:10.1021/acsenergylett.0c00039.
8. Xie F. X., Zhang D., Su H., Ren X., Wong K. S., Grätzel M., Choy W. C. H., ACS Nano, 2015, **9**, No. 1, 639–646, doi:10.1021/nn505978r.
9. Chen H., Lü Z., Liu Z., Wu Y., Wang S., Wang Z., RSC Adv., 2023, **13**, 28382, doi:10.1039/D3RA05026B.
10. Wang J., Gao Y., Ciucci F., ACS Appl. Energy Mater., 2018, **1**, 6409, doi:10.1021/acsaem.8b01365.
11. Meng W., Saparov B., Hong F., Wang J., Mitzi D. B., Yan Y., Chem. Mater., 2016, **28**, 821, doi:10.1021/acs.chemmater.5b04213.
12. Jin G. B., Choi E. S., Guertin R. P., Brooks J. S., Booth C. H., Albrecht-Schmitt T. E., Inorg. Chem., 2007, **46**, 9213, doi:10.1021/ic701012j.
13. Sun Y. Y., Agiorgousis M. L., Zhang P., Zhang S., Nano Lett., 2015, **15**, 581, doi:10.1021/nl504046x.
14. Kaur P., Singh K., Ionics, 2020, **26**, 6233, doi:10.1007/s11581-020-03752-w.
15. Monama G. R., Ramohlola K. E., Iwuoha E. I., Modibane K. D., Results Chem., 2022, **4**, 100321, doi:10.1016/j.rechem.2022.100321.
16. Giannozzi P., Baroni S., Bonini N., Calandra M., Car R., Cavazzoni C., Ceresoli D., Chiarotti G. L., Cococcioni M., Dabo I., et al., J. Phys.: Condens. Matter., 2009, **21**, 395502, doi:10.1088/0953-8984/21/39/395502.
17. Perdew J. P., Burke K., Ernzerhof M., Phys. Rev. Lett., 1996, **77**, 3865, doi:10.1103/PhysRevLett.77.3865.
18. Floris A., Timrov I., Himmetoglu B., Marzari N., de Gironcoli S., Cococcioni M., Phys. Rev. B, 2020, **101**, 064305, doi:10.1103/PhysRevB.101.064305.
19. Hamann D. R., Phys. Rev. B, 2013, **88**, 085117, doi:10.1103/PhysRevB.88.085117.
20. Monkhorst H. J., Pack J. D., Phys. Rev. B, 1976, **13**, 5188, doi:10.1103/PhysRevB.13.5188.
21. Pfrommer B. G., Côté M., Louie S. G., Cohen M. L., J. Comput. Phys., 1997, **131**, 233, doi:10.1006/jcph.1996.5612.
22. Motornyi O., Raynaud M., Dal Corso A., Vast N., J. Phys.: Conf. Ser., 2018, **1136**, 012008, doi:10.1088/1742-6596/1136/1/012008.
23. Madsen G. K. H., Singh D. J., Comput. Phys. Commun., 2006, **175**, 67, doi:10.1016/j.cpc.2006.03.007.
24. Goldschmidt V. M., Die G., Naturwissenschaften, 1926, **14**, 477, doi:10.1007/BF01507527, (in German).
25. Murnaghan F. D., Proc. Natl. Acad. Sci. U.S.A., 1944, **30**, 244, doi:10.1073/pnas.30.9.244.
26. Agrawal A., Meredig B., Wolverton C., Choudhary A., In: 2016 IEEE 16th Int. Conf. Data Min. Workshop ICDMW, IEEE, Barcelona, Spain, 1276–1279, doi:10.1109/ICDMW.2016.0183.
27. Freysoldt C., Grabowski B., Hickel T., Neugebauer J., Kresse G., Janotti A., Van de Walle C. G., Rev. Mod. Phys., 2014, **86**, 253, doi:10.1103/RevModPhys.86.253.
28. Luan X., Qin H., Liu F., Dai Z., Yi Y., Li Q., Crystals, 2018, **8**, 307, doi:10.3390/cryst8080307.
29. Karki B. B., Ackland G. J., Crain J., J. Phys.: Condens. Matter., 1997, **9**, 8579, doi:10.1088/0953-8984/9/41/005.

30. Mouhat F., Coudert F. X., Phys. Rev. B., 2014, **90**, 224104, doi:10.1103/PhysRevB.90.224104.
31. Walpole L. J., Adv. Appl. Mech., 1981, **21**, 169, doi:10.1016/S0065-2156(08)70332-6.
32. Hill R., Proc. Phys. Soc. A, 1952, **65**, 349, doi:10.1088/0370-1298/65/5/307.
33. Ravindran P., Fast L., Korzhavyi P. A, Johansson B., Wills J., Eriksson O., J. Appl. Phys., 1998, **84**, 4891, doi:10.1063/1.368733.
34. Pugh S. F., Philos. Mag., 1954, **45**, 823, doi:10.1080/14786440808520496.
35. Kumar S., Jung J., Mater. Sci. Eng., B, 2013, **178**, 10, doi:10.1016/J.MSEB.2012.10.003.
36. Ranganathan S. I., Ostoja-Starzewski M., Phys. Rev. Lett., 2008, **101**, 055504, doi:10.1103/PhysRevLett.101.055504.
37. Long J., Yang L., Wei X., J. Alloys Compd., 2013, **549**, 336, doi:10.1016/j.jallcom.2012.08.120.
38. Shang S., Wang Y., Kim D., Liu Z., Comput. Mater. Sci., 2010, **47**, 1040, doi:10.1016/j.commatsci.2009.12.006.
39. Kassa M. D., Debelo N. G., Woldemariam M. M., Indian J. Phys., 2024, **98**, 1259, doi:10.1007/s12648-023-02905-7.
40. Walker B., Saitta A. M., Gebauer R., Baroni S., Phys. Rev. Lett., 2006, **96**, 113001, doi:10.1103/PhysRevLett.96.113001.

Дослідження перовскіту $LaBiO_3$ для фотоелектричних, термоелектричних та оптоелектронних застосувань

М. М. Волдемаріам, Н. Г. Дебело, Т. К. Туфа, Е. М. Гурмеса, С. Х. Діду, С. Н. Асфав, Д. Т. Кено

Фізичний факультет університету Джимми, п/с 378, Джимма, Ефіопія

Використовуючи теорію функціоналу густини (DFT) з псевдопотенціалом ONCVVPSP та функціоналом PBE, досліджуються структурні, електронні, пружні, оптичні та термоелектричні властивості тригонального перовскітного оксиду $LaBiO_3$ (просторова група R3c). За допомогою рівняння стану були визначені параметри основного стану: стала ґратки, об'єм, модуль об'ємної пружності та його похідна за тиском. Застосування поправки Хаббарда (GGA+U) виявило непряму широку заборонену зону 3.51 еВ. Механічні властивості, включаючи коефіцієнт анізотропії, модуль пружності та коефіцієнт Пуассона, були розраховані за схемою усереднення Фойгта-Ройса-Хілла. Відношення модуля об'ємної пружності до модуля зсуву ідентифікує тригональну фазу як пластичну. Крім того, були обчислені температури Дебая та швидкості звуку. Оптичні характеристики (коефіцієнт поглинання, показник заломлення та функція втрат енергії електронів) були оцінені в спектральному діапазоні 0–35 еВ. Для оцінки термоелектричного потенціалу матеріалу були розраховані напівкласичні коефіцієнти переносу, включаючи електропровідність, коефіцієнт Зеєбека та коефіцієнт потужності.

Ключові слова: *теорія функціоналу густини, $LaBiO_3$, електронні властивості, пружні властивості, оптичні властивості, транспортні властивості*